GPS Availability and Positioning Issues When the Signal Paths are Aligned with Ionospheric Plasma Bubbles

Alison de O. Moraes

Instituto de Aeronáutica e Espaço - IAE / Instituto Tecnológico de Aeronáutica - ITA

São José dos Campos, SP, Brazil

alisonaom@iae.cta.br

Bruno C. Vani

Instituto Federal de Educação, Ciência e Tecnologia de São Paulo - Campus Presidente Epitácio (IFSP-PEP) /Universidade Estadual Paulista Júlio de Mesquita Filho - UNESP

Presidente Epitácio, SP/ Presidente Prudente, SP, Brazil,

brunovani@ifsp.edu.br

Emanoel Costa

Centro de Estudos em Telecomunicações, Pontifícia Universidade Católica do Rio de Janeiro (CETUC/PUC-Rio), Rua Marquês de São Vicente 225, 22451-900 Rio de Janeiro, RJ, Brazil

epoc@cetuc.puc-rio.br

Mangalathayil A. Abdu

*Instituto Tecnológico de Aeronáutica - ITA/*Instituto Nacional de Pesquisas Espaciais – INPE, São José dos Campos, SP, Brazil

ma.abdu@inpe.br

Eurico R. de Paula

Instituto Nacional de Pesquisas Espaciais – INPE, São José dos Campos, SP, Brazil

eurico.paula@inpe.br

Jonas Sousasantos

Instituto Tecnológico de Aeronáutica - ITA

São José dos Campos, Brazil

jonasjss@ita.br

João F. G. Monico

Universidade Estadual Paulista Júlio de Mesquita Filho - UNESP, Presidente Prudente, SP, Brazil

galera@fct.unesp.br

Biagio Forte

University of Bath – Bath, United Kingdom

B.Forte@bath.ac.uk

Patrícia Mara de Siqueira Negreti

Instituto Nacional de Pesquisas Espaciais – INPE, São José dos Campos, SP, Brazil

São José dos Campos, Brazil

patricia.mara@dae.inpe.br

Milton Hirokazu Shimabukuro

Universidade Estadual Paulista Júlio de Mesquita Filho - UNESP

Presidente Prudente, SP, Brazil, miltonhs@fct.unesp.br

Formatted: Portuguese (Brazil)

Formatted: Portuguese (Brazil)

Formatted: Portuguese (Brazil)

Abstract The propagation paths of signals through equatorial ionospheric irregularities are analyzed by evaluating their effects on Global Navigation Satellite System positioning and availability. Based on observations during 32 days by a scintillation monitor at São José dos Campos, Brazil, it was noted that there is a dominance of enhanced scintillation events for Global Positioning System ray paths aligned with the azimuth angle of 345º (geographic northwest). This azimuth corresponds to the magnetic meridian that has a large westward declination angle in the region (21.4º W). Such results suggest that the enhanced scintillation events were associated with Global Positioning System signals that propagated along the direction of the magnetic field aligned plasma bubbles; in other words head-on through the plasma bubbles. It will be shown that, under this alignment condition, the longer propagation path length through plasma bubbles can result in more severe scintillation cases and more losses of signal lock, as supported by proposed statistics of bit error probability and mean time between cycle slips. Additionally, large precise positioning errors are also related to these events, as demonstrated by Precise Point Positioning experiments.

Formatted: Portuguese (Brazil)

Introduction

Ionospheric scintillation degrades the accuracy of navigation and positioning based on Global Navigation Satellite Systems (GNSS). Some authors observed that rapid phase variations are mapped into Doppler shifts in the Global Positioning System (GPS) signal, which may exceed the bandwidth of the phase lock loop, resulting in a loss of phase lock (Doherty et al. 2004). Additionally, amplitude fades may cause the signal-to-noise ratio to drop below the receiver threshold. These effects often accompany propagation delays and increase range measurement errors, besides causing the carrier and code loops to lose lock (Kintner et al. 2001). Scintillation may seriously affect positioning, resulting in total disruption of the receiver operation (Basu and Basu 1981). Such extreme phenomena are more usual near the equatorial and low-latitude regions (between ±20º geomagnetic latitude) than in the auroral and polar zones (above 55º latitude). This work analyzes GPS scintillation data recorded during 32 days of the current solar maximum conditions at São José dos Campos, Brazil (geographic coordinates: 23.2º S, 45.9º W, dip latitude: 19.2º S), near the southern crest of the Equatorial Ionization Anomaly (EIA). The analysis has been performed by relating the scintillation intensity with the geometry of the propagation paths through the ionospheric irregularities and then evaluating the effects on GPS positioning and availability. The nature of the plasma bubble irregularity distribution with respect to the geomagnetic field configuration may magnify the scintillation effects. In Brazil, the geomagnetic field configuration, characterized by a large magnetic declination angle, provides a particular and favorable condition to assess such effects. A recent study by Moraes et al. (2017) showed scintillation enhancement events around the azimuth angle of 345º, which corresponds to signal propagation along ray paths that are nearly aligned with the magnetic meridian in this region. In view of the large westward magnetic declination (21.4º W) of the region, this result suggested that the enhanced scintillation events were associated with GPS signals that propagated along the direction of the magnetic field aligned plasma bubbles. Calculations of the propagation angles with respect to the magnetic field lines showed that small values of this parameter and the larger propagation path length through bubbles could result in severe scintillation and more cases of loss of phase lock. This analysis will also show that large errors on Precise Point Positioning (PPP) are related to the eventual alignment.

Recently, Humphreys et al. (2009; 2010a) have suggested that deep fades in the amplitude of received signals, simultaneously occurring with sudden phase changes, caused loss

of phase lock in carrier tracking loops of GPS receivers. Such occurrences, also known as "canonical fades", have been observed during strong low-latitude scintillation events (Humphreys et al. 2010b). In the present work, the canonical fading will be examined as a likely consequence of GPS signal propagation paths being aligned with the plasma bubble. These nonlinear ionospheric propagation effects on the GPS radio signal will be analyzed using the fading coefficients of the α-μ distribution (Yacoub 2007).

The next section will survey ionospheric scintillation. After a brief description of the experimental setup, the period of analysis and the geophysical condition will be presented. In sequence, a formulation that estimates the mean time between cycle slips in the receiver tracking loop will be presented, based on its observed relation with the bit error probability (Humphreys et al. 2010b). Next, the relation between scintillation parameters and propagation path directions will be analyzed and evidences of the effects of this irregularity alignment on the GPS Precise Point Positioning will be presented. The final section summarizes the main results in the study and presents concluding remarks.

The scintillation-producing ionospheric irregularities

Plasma irregularities may develop in the post-sunset equatorial ionosphere under the electrodynamics processes unique to the sunset transition. The pre-reversal enhancement in the evening zonal electric field causes rapid uplifts of the steep gradient region of the bottomside ionospheric F layer. This establishes the conditions for the interchange instability processes driven by the Rayleigh-Taylor (R-T) mechanism to act on density perturbations, which begin to grow. The nonlinear growth of the irregularities involves the bottomside lower density plasma rising up even further to the topside ionosphere, in the form of magnetic flux tube aligned plasma depletions (known as equatorial plasma bubbles, EPBs), with extremities extending to latitudes of larger background plasma density in the Equatorial Ionization Anomaly. During their evolution, the EPBs are observed to drift generally eastward. Motions of medium-scale density secondary structures across transionospheric paths form complex moving field patterns at the ground that contain amplitude and phase variations. In this way, random temporal fluctuations are produced in both amplitude and phase of satellite signals received at the ground, which are

known as amplitude and phase scintillations, respectively (Yeh and Liu 1982). The irregularities with scale sizes of a few hundred meters are responsible for producing scintillation of transionospheric signals emitted by GNSS satellites (Kintner et al. 2007). Under geomagnetically quiet conditions, the equatorial scintillation activity develops in the post-sunset hours and typically lasts for 4-5 hours until midnight, sometimes also extending for a few hours into the post-midnight period. It presents strong seasonal and longitudinal variations that are dependent on the corresponding variations in the alignment between the sunset terminator and the magnetic meridian, as well as on the availability of seeding sources (Abdu et al. 1981; Tsunoda 1985). In the Brazilian region, scintillation activity extends from September to March and peaks around December. In addition, short-term variability may occur due to upward propagating atmospheric waves, sudden stratospheric warming episodes, and changes in solar and magnetic activities (de Paula et al. 2015; Abdu et al. 2015).

EPBs have east-west extension of a few tens to hundreds of kilometers and often occur in succession with zonal separation of a few hundred kilometers. Such features may be noted as the magnetic north-south aligned depletion patches in the total electron content (TEC, with units of 10^{16} el/m^2) distribution map constructed from measurements using GPS receiver arrays. Some examples of such TEC maps over Brazil, using data from 17 to 28 November 2014, are shown in Figure 1. Note that the TEC depletions (valley regions), associated with equatorial plasma bubbles, extend from the EIA trough region (along the dip equator) to the EIA crest region of (red and brown) larger background TEC values. We also note a large degree of day-to-day variability in the TEC depletions, as well as in the background TEC values. Two situations lead to intense scintillation. The first is the presence of the larger background plasma density that exists in the crest region of the Equatorial Ionization Anomaly, where the plasma irregularities are more intense. The second situation, which is the focus of the present study, is the degree to which segments of signal propagation paths become closer to being aligned with the field-aligned plasma bubble structures. Since scintillation results from effects integrated along the propagation path, the longer the field-aligned propagation segment, the more intense will the amplitude (or phase) scintillation be. In other words, the geomagnetic declination and inclination angles associated with the GPS propagation path 350-km Ionospheric Pierce Point (IPP) distribution are controlling factors of the scintillation distribution surrounding a receiving site.

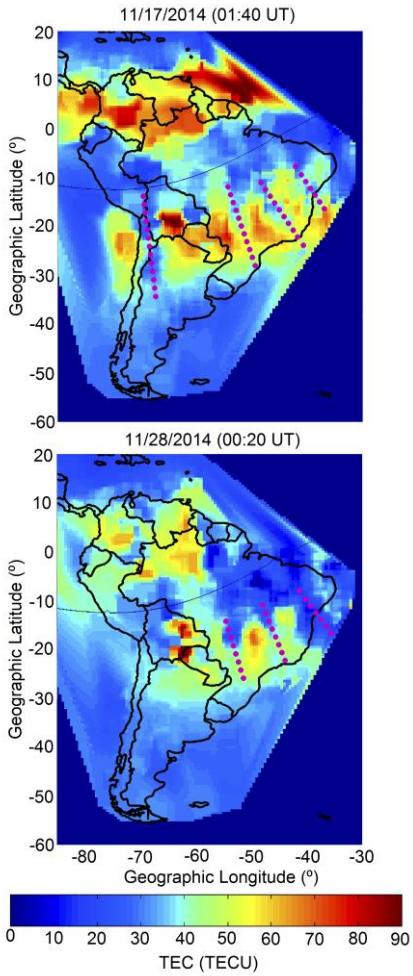

Fig. 1 Examples of TEC maps over Brazil, showing the magnetic north-south aligned bubble structures (pink dots) with extremities extending several degrees to lower geomagnetic latitudes. Also shown are (red and brown) larger background TEC values in the EIA crest region.

Ionospheric scintillation measurements, spatial distribution and alignment

The scintillation data used in the present study were recorded by a Septentrio PolaRxS monitor belonging to the CIGALA/CALIBRA network (Vani et al. 2016). This monitor is located at São José dos Campos (SJC), Brazil (geographic coordinates: 23.2º S, 45.9º W, dip latitude: 19.2º S). The analysis focuses on two periods: 15-30 November 2014 and 04-18 February 2015. The average sunspot number and the F10.7 solar flux values varied around 169 and 133 s.f.u. (1 s.f.u. = 10^{-22} W/m^2/Hz), respectively. The measurements were made during the equatorial spread F occurrence season in Brazil, which typically extends from September to April (Sobral et al. 2002). For this study, GPS satellites with elevations greater than 20° were considered. In the set of observations from 19:00 LT to 01:00 LT during 32 nights, approximately 179 hours of significant GPS L1 amplitude scintillation were recorded, considering the transmissions from all satellites.

The strength of the amplitude scintillation, represented by the S_4 index, defined as the normalized standard deviation of the received signal intensity (Yeh and Liu 1982)

$$S_4 = \sqrt{\langle I^2 \rangle - \langle I \rangle^2} \Big/ \langle I \rangle \quad (1)$$

is one of the basic parameters for this study. In this well-known expression, $I = |R|^2$ is the received intensity signal, R is its amplitude, and < > denote an ensemble average during one minute. The receiver records the intensity at 50 Hz for all tracked satellites, providing the respective S_4 index at every 60 seconds. Only samples with $S_4 > 0.3$ were considered as scintillation cases. The first Fresnel zone scale sizes of the field-aligned irregularities that are responsible for scintillation, immersed in the larger-scale plasma bubbles, are approximately equal to 400 meters at the GPS L-band frequencies.

Figure 2 shows the azimuth and elevation distributions of amplitude scintillation observed by the São José dos Campos monitor during the two periods of observations. All 10743 scintillation cases with $S_4 > 0.3$ were used in this plot. The top panel of Figure 2 shows azimuth-elevation distribution of the S_4 values in association with the 350-km IPPs, using the color scale on the right to represent the scintillation strength. Note that consecutive orbits show very small day-to-day variations during the period of observation. To emphasize the severity of scintillation effects on GPS transmissions, the highest S_4 values were brought to front in this plot, showing the predominance of moderate-to-strong amplitude scintillation levels with $S_4 > 0.9$ in the

198 northern sector. This feature may be partly due to the ambient plasma density, since TEC must
199 be stronger in the northern sector over São José dos Campos, which includes the crest of the
200 EIA. Scintillation is highly dependent on the apex altitude of the irregularities. The apex
201 altitudes, corresponding to the aligned cases in the northern sector, vary from 431 km to 556 km.
202 Equatorial plasma bubbles commonly reach these apex altitudes over Brazil (Abdu et al. 2009).
203 In principle, bubble irregularities may also extend to regions southward of the receiving site.
204 However, only weak signatures of such bubble irregularities were observed in the available data
205 set.

206 The middle and bottom bar charts in Figure 2 represent the elevation and azimuth
207 distributions of scintillation occurrences for S_4 values varying from $0.3 \leq S_4 < 0.5$ to $S_4 > 1.1$.
208 Note that 80% of the cases with $S_4 \geq 1.1$ are associated with elevations less than 41^o. For $0.9 \leq S_4$
209 <1.1 and $0.7 \leq S_4 <0.9$ and the same elevation interval, the corresponding percentages are 75%
210 and 73 %, respectively. The azimuth chart confirms in quantitative terms the predominance of
211 high S_4 values between azimuths 315^o and 360^o. For this azimuth sector, $S_4 \geq 1.1$, $0.9 \leq S_4 < 1.1$,
212 and $0.7 \leq S_4 < 0.9$ make up 68%, 62%, and 40% of the observed data, respectively. These results
213 are consistent with the ones provided by Xu et al. (2012).

214

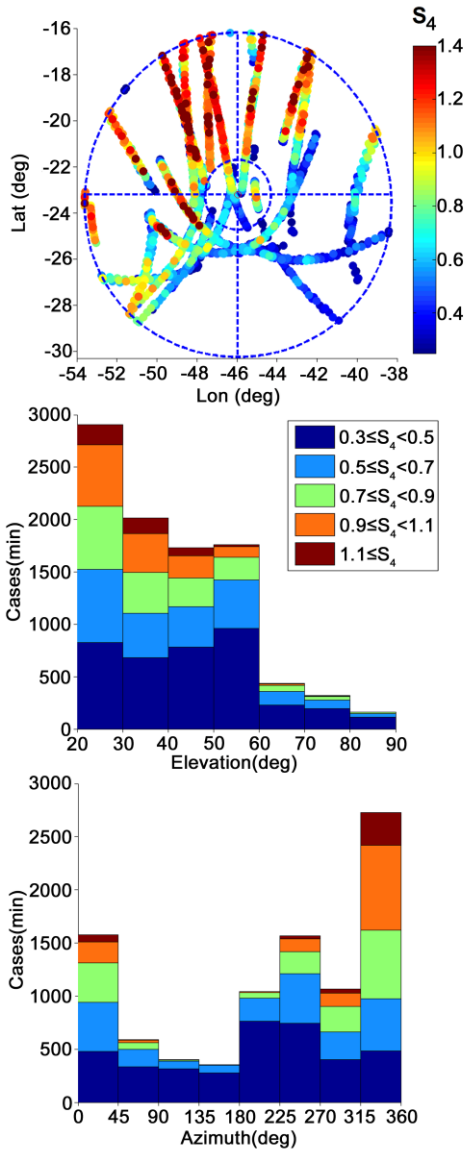

215

216 **Fig. 2** GPS L1 amplitude scintillation events plotted at the respective IPP values (top panel). The
217 outer and inner circles define elevations of 20º and 60º. The middle and bottom panels show S_4
218 distributions as functions of elevation and azimuth, respectively.

Cycle slips, bit error rate and α-μ model

Humphreys et al. (2010b) showed that the bit error probability P_e for binary differential phase-shift keying (binary DPSK) transmissions and the mean time between cycle slips T_s are closely related by $T_s \approx T_b / P_e$, where T_b = 0.02 s is the GPS L1 bit duration. Based on this connection, and assuming a Ricean fading channel, they proposed a model for estimating the cycle slip rate as a function of scintillation intensity, the fluctuation speed, and the carrier power to noise power density ratio.

Based on the work of Yacoub (2007), Moraes et al. (2012; 2014a) used the α-μ model to provides a flexible and realistic description of the amplitude scintillation. The α-μ probability density function (pdf) of the amplitude envelope R of the received signal is given by

$$f_R(r) = \frac{\alpha\ \mu^{\mu}}{\Gamma(\mu)\tilde{r}} (r/\tilde{r})^{\alpha\mu-1} \exp\left[-\mu(r/\tilde{r})^{\alpha}\right] \tag{2}$$

where $\alpha > 0$ is an arbitrary fading parameter, $\tilde{r} = \left[E\left(R^{\alpha}\right)\right]^{1/\alpha}$, and $\mu > 0$ is the inverse of the normalized variance of R^{α}; that is, $\mu = E^2(R^{\alpha})/\{E(R^{2\alpha})-E^2(R^{\alpha})\}$. Additionally, $\Gamma(z)$ is the Gamma function of the argument z.

Based on the evidence provided by Humphreys et al. (2010b) and considering binary DPSK transmissions, P_e, and consequently T_s, will be estimated by using the α-μ model. To compute P_e, the α-μ probability density function (pdf) of the instantaneous signal-to-noise ratio $S = \tilde{s}(R/\tilde{r})^2$, where $\tilde{s} = \tilde{r}^2(E_b/N_o)$, and (E_b/N_o) is the energy per bit to noise power density ratio, is initially obtained from (2) by a straightforward derivation (Magableh and Matalgah 2009)

$$f_S(s) = \frac{\alpha\mu^{\mu}}{2\Gamma(\mu)\tilde{s}} (s/\tilde{s})^{\alpha\mu/2-1} \exp\left[-\mu(s/\tilde{s})^{\alpha/2}\right] \tag{3}$$

Note that $(E_b/N_o) = T_b(C/N_o)$. Considering $E(R^2) = 1$, one gets

$$\tilde{r}^2 = \frac{\mu^{2/\alpha}\Gamma(\mu)}{\Gamma(\mu+2/\alpha)} \quad \rightarrow \quad \tilde{s} = \frac{\mu^{2/\alpha}\Gamma(\mu)}{\Gamma(\mu+2/\alpha)}(E_b/N_o) = \left[\frac{\mu^{2/\alpha}\Gamma(\mu)}{\Gamma(\mu+2/\alpha)}\right] T_b(C/N_o) \tag{4}$$

For binary DPSK, P_e is given by (El Ayadi and Ismail 2014)

$$P_e = \int_0^{\infty} \frac{1}{2} \exp(-s)\, f_S(s)\, ds \tag{5}$$

Combining (3) to (5) and changing the integration variable, P_e can be computed by

$$P_e = \frac{\alpha \mu^{\mu}}{4\Gamma(\mu)} \int_0^{\infty} v^{\alpha\mu/2-1} e^{-\left(\mu v^{\alpha/2} + \tilde{s} v\right)} dv \tag{6}$$

Several formulations for P_e calculation have generally adopted the moment generating function (MGF) approach to express their final results in closed forms, in terms of transcendental functions (Magableh and Matalgah 2009; El Ayadi and Ismail 2014). However, (6) may be easily and accurately calculated by numerical quadrature methods.

The left panels of Figure 3, obtained from (6) through the latter approach, illustrate the dependence of P_e as a function of C/N_o, for S_4 = 1.1 (upper left), S_4 = 0.8 (lower left), and different values of (α, μ, and $\tilde{r}$). By using the α-μ model, it is more intuitive to analyze scintillation based on S_4, having α as an auxiliary severity indicator. Indeed, Moraes et al. (2014b) established the following relation between the scintillation index S_4 and the parameters of the α-μ distribution

$$S_4^{\,2} = \frac{\Gamma(\mu)\Gamma(\mu + 4/\alpha) - \Gamma^2(\mu + 2/\alpha)}{\Gamma^2(\mu + 2/\alpha)} \tag{7}$$

This equation numerically leads to a μ value for each pair of independent parameters S_4 and α, and the associated $\tilde{r}$) value is immediately obtained from equation (4). Equation (7) indicates that the α-μ model may describe different scintillation patterns for each value of S_4. This is especially interesting for strong scintillation, since it is well known that S_4 alone does not describe the effects from ionospheric perturbations on GPS signals. Each of the left panels of Figure 3 (with legends displaying, for fixed values of S_4 and selected α values, the calculated number for μ and $\tilde{r}$), confirms this information. As expected, the panels show that P_e decreases as S_4 increases and each curve shows that the bit error probability P_e decreases as C/N_o increases (and vice-versa). However, for C/N_o = 42 dB-Hz and S_4 = 1.1, the estimated values for P_e on the upper-left panel of Figure 3 are 2.1×10^{-4}, 3.8×10^{-3} and 1.4×10^{-2}, for α = 1.0, 2.0 (the Nakagami-

m case) and 3.5, respectively. For $S_4 = 0.8$, the corresponding estimates on the bottom-left panel of Figure 3 are 2.0×10^{-6}, 1.3×10^{-4}, and 1.3×10^{-3}, for $\alpha = 1.0$, 2.0, respectively.

The right panels of Figure 3 simply map P_e into the mean time between cycle slips through the approximate relationship $T_s \approx T_b / P_e$. Correspondingly, these panels show that T_S decreases as S_4 increases and each curve shows that T_S increases as C/N_o also increases (and vice-versa). It is also possible to observe the influence of S_4, C/N_o, and α on the cycle slip occurrence. Considering $C/N_o = 42$ dB-Hz and $S_4 = 1.1$, the estimated values of T_S are 94.90 s, 5.33 s and 1.48 s, for $\alpha = 1.0$, 2.0 and 3.5, respectively. For $S_4 = 0.8$, the corresponding estimates are 9.53×10^3 s, 1.61×10^2 s and 1.55×10^1 s. The above results illustrate how signals with similar S_4 and C/N_o may have completely different effects on P_e and T_s.

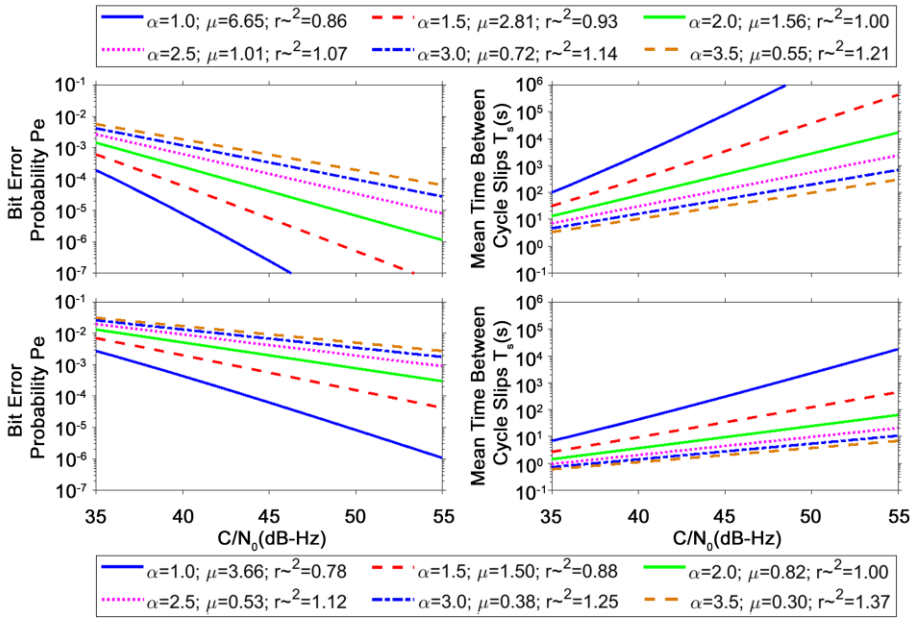

Fig. 3 Curves for P_e (left panels) and T_s (panels) as functions of C/N_o and different values of α (and associated values of μ and $\tilde{r}$). The upper and bottom panels assume $S_4 = 1.1$ and $S_4 = 0.8$, respectively.

Formatted: English (United States)

In addition to S_4 and average C/N_o, the scintillation monitor records a flag indicating whether cycle slips occurred during the one minute of high-resolution (50 Hz) measurements. The estimated values of α, μ, P_e and T_s are also associated with each one-minute record. Figure 4 displays the estimated T_s for the records in which cycle slips occurred, with each symbol representing the corresponding values of S_4, α, and T_s. For a fixed value of S_4 (± 0.025), each scattered plot relates T_s to α, reinforcing that: (1) on average, T_s decreases with increasing values of S_4; and (2) for a fixed value of S_4, an increase in α indicates an increase in the number of fades and an associated decrease in T_s (Moraes et al. 2014a). The observed dispersion in T_s for fixed values of S_4 and α is due to variations in C/N_o. It should be remembered that the Septentrio PolaRxS GPS monitor is not a standard configuration. Instead, it is optimized for tracking through periods of scintillation. Thus, the above distribution of cycle slips is very likely different from those of normal GPS receivers in quantitative terms. However, it is expected that the qualitative principles extracted from the above results would also be applicable to them.

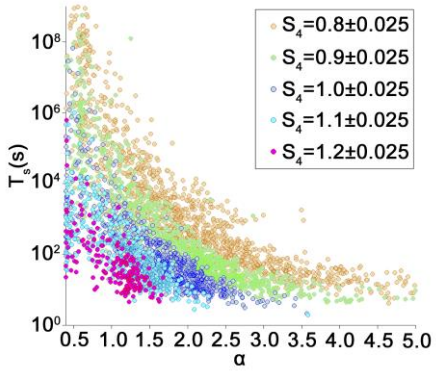

Fig 4 Cycle slips detected by the scintillation monitor for different S_4 (± 0.025) ranges.

Alignment and Availability

This section associates P_e and T_s with the angle between the propagation path and the geomagnetic field directions. To obtain this angle, the propagation path direction lines (in terms

of their azimuth and elevation angles) at the 350-km IPPs were initially calculated for the receiver location and all satellite positions at that moment. The latest version of the International Geomagnetic Reference Field (*IGRF-12*) (Thébault et al. 2015) provided the geomagnetic field line directions at the IPPs. Next, all determined lines were projected onto the vertical (north and up) and horizontal (north and east) planes at the IPPs. The first projection (ω) measures the difference between the path elevation and the geomagnetic inclination. Note that the path elevations at the IPPs displayed by Figure 2, measured from the horizontal plane toward zenith at the IPP, are always greater than 20^o, as explained in the first paragraph of the third section. Similarly, the geomagnetic inclination line is also above the same horizontal plane, since the dip angle is negative in the southern hemisphere. However, the difference ω can be negative or positive, indicating that the path elevation line is below or above the geomagnetic inclination line, with respect to that horizontal plane, respectively. The second projection (ν) represents the angle between the path azimuth and the geomagnetic declination lines on the horizontal plane through the IPP. While the path azimuths at the IPPs displayed by Figure 2 vary from 0^o to 360^o, the angle ν can be negative, indicating that the path azimuth line is to the right of the geomagnetic declination line, or positive, if the other relative position holds. Thus, the set of parameters associated with each one-minute record, listed in the last paragraph of the previous section, is augmented with ω and ν. The present study assumed that if $|\omega|$ and $|\nu|$ are simultaneously less than 10^o, the GPS propagation path would be effectively aligned with the ionospheric bubble irregularity structure.

The bar plots in the top and middle panels of Figure 5 display the number of L1 scintillation occurrences as a function of ω and ν, for different ranges of S_4. It is noted that the smallest ω are related with the largest scintillation index interval, and vice-versa. Similarly, the largest S_4 values occur when the difference between the propagation angle and the magnetic declination is the smallest. Thus, a small angle between the propagation direction and the field-aligned bubbles, on both vertical and horizontal planes, corresponds to large scintillation intensity. The bottom panel of Figure 5 shows the percentages of aligned and nonaligned cases, which always add to 100 % within each S_4 interval. It indicates that the increasing percentage of alignment between the propagation angle and magnetic field line results in a severe increase of the scintillation intensity.

335 The top panel of Figure 6 shows the estimated T_s values as functions of S_4, where the
336 colors red and green represent aligned and nonaligned cases, respectively. It is noticed that the
337 aligned cases are concentrated in the region of high S_4 and low T_s values. The bottom panel in
338 Figure 6 shows the percentages of aligned and nonaligned cases for different T_s classes. Again,
339 the two percentages associated with each class add to 100 %. For very rare occurrences of cycle
340 slips (48 h < $T_S \leq$ 168 h, corresponding to one such event within the interval from two days to
341 one week), the percentage of aligned cases is only 5.6%. This percentage increases to 18.5% for
342 T_S between 5 min and 20 min. However, for 1 s < T_s < 10 s, the percentage of aligned cases
343 reaches 30.7%. Therefore, the alignment between the propagation path and the geomagnetic field
344 directions favors the occurrence of the most serious conditions for the GPS receiver operation,
345 leading to high values of S_4 and small values of T_S.
346
347

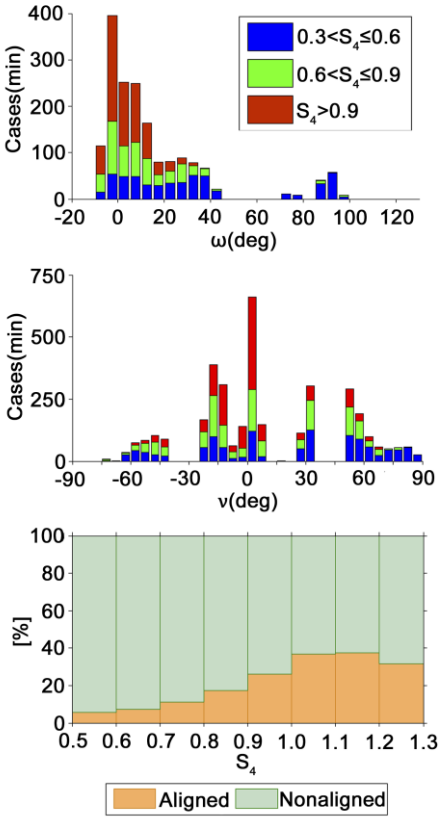

Fig. 5 Top and middle panels: number of L1 scintillation occurrences as a function of ω and ν, respectively, for different ranges of S_4 values. Bottom panel: percentages of alignment and nonalignment as functions of S_4 intervals. Note that, for all S_4 intervals, the two percentages always add to 100 %.

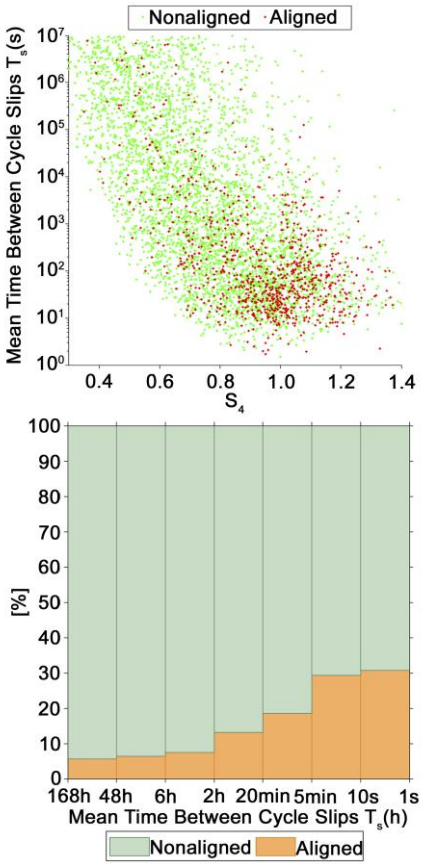

Fig. 6 Top panel: scatter plot of the mean time between cycle slips T_s as a function of S_4 for of aligned and nonaligned cases. Bottom panel: percentages of aligned and nonaligned cases for different T_s classes. Note that, for all T_s classes, the two percentages always add to 100 %.

Figure 7 displays the histograms for ω and ν, conditioned by $T_s < 200$ s. They show the concentration of the most likely cases of loss of lock around 0^o for both angles ω and ν. The percentages of S_4 classified by the alignment in Figure 5 and the present plots show that GPS signals received end-on through field aligned plasma bubbles may suffer enhancement in

scintillation intensity. In view of the inverse relationship between T_s and S_4, evident in the top panel of Figure 6, the distributions of the numbers of cases of T_s < 200s with respect to ω and ν, which show their maximum occurrences at small angles, are consistent with top and middle panels of Figure 5. Such enhancement appears in addition to that occurring in the EIA crest region, arising from the fountain effect on the background plasma density. Scintillation enhancements due to the EIA crest region (to the north of the GPS receiver) may also contribute to the alignment effect seen on the vertical plane; that is, as a function of ω. However, the cases of enhanced scintillation intensity ~~and those of~~in which T_s < 200s for propagation alignment in azimuth ν do represent the scintillation enhancement for ~~end on~~a case ~~view~~ where ~~unaff~~ the~~ected by~~ EIA crest effect is smaller. Both effects make signal tracking more difficult, with direct impact on the performance and availability of GPS receivers.

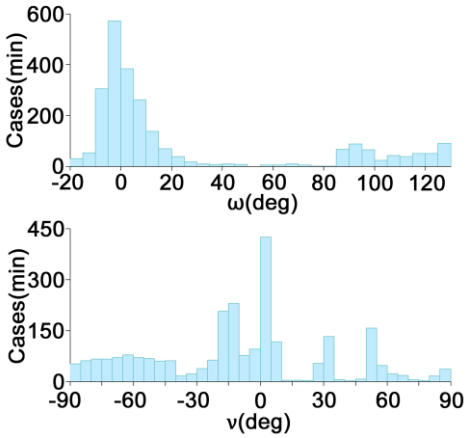

Fig. 7 Top panel: distribution of the angular difference between the path elevation and magnetic inclination (dip angle) for T_s < 200 s. Bottom panel: distribution of the value of the angular difference between the path azimuth and the geomagnetic declination for T_s < 200 s.

Table 1 presents the average and standard deviation values of α, as well as its maximum recorded value for different S_4 intervals, considering aligned and nonaligned cases. It also presents the number of analyzed cases in each class. The analysis considers only the one-minute

records affected by losses of lock, as indicated by the corresponding flag. It is observed that the average value of α for each aligned case is greater than the one for the corresponding nonaligned case. For all S_4 intervals, the increase of α values implies a decrease in the estimate of T_s as shown in Figure 3. This is an indication that the alignment affects the statistics of amplitude scintillation in a severe way, with distributions that display a higher percentage of deep fades than those related with the nonaligned ones (Moraes et al. 2014b).

Table 1 Comparison between statistics of α coefficients for aligned and nonaligned conditions.

	Aligned				Nonaligned			
	E(α)	std(α)	max(α)	Cases	E(α)	std(α)	max(α)	Cases
$0.3<S_4\leq0.4$	3.16	4.37	51.20	42	2.58	2.59	22.93	2151
$0.4<S_4\leq0.5$	2.72	3.08	20.54	55	2.34	2.66	48.05	1549
$0.5<S_4\leq0.6$	3.14	3.62	23.66	69	2.16	2.27	22.39	1176
$0.6<S_4\leq0.7$	2.91	3.18	30.55	69	2.28	2.28	18.21	890
$0.7<S_4\leq0.8$	2.83	2.70	22.16	91	2.21	1.67	13.74	733
$0.8<S_4\leq0.9$	2.58	3.48	56.48	133	1.99	3.28	52.07	635
$0.9<S_4\leq1.0$	2.01	1.09	12.38	188	1.82	3.13	43.86	534
$1.0<S_4\leq1.1$	1.15	0.67	3.68	207	1.15	0.62	2.53	357
$1.1<S_4\leq1.2$	1.02	0.48	2.20	100	0.90	0.44	1.68	166
$1.2<S_4$	0.81	0.37	1.62	57	0.65	0.34	1.40	123

This section showed that GPS signals propagating along the magnetic field lines are more likely to propagate longer distances in the turbulent medium created by the field-aligned EPBs. Therefore, the alignment geometry is more likely to cause interruptions to GPS receiver operation.

Alignment and Positioning

This section discusses the influence of ionospheric irregularity alignments with the signal propagation paths on GPS positioning. The observation dataset was evaluated by the Precise Point Positioning (PPP) approach (Zumberge et al. 1997) using the RT-PPP software developed by the Universidade Estadual Paulista Júlio de Mesquita Filho (UNESP), available at <http://is-cigala-calibra.fct.unesp.br/ppp/> (Marques 2014).

The PPP was applied with the standard configuration (that is, with corrections for tropospheric and first-order ionospheric refraction effects, but without any attempt to mitigate those from scintillation). Dual-frequency (L1 and L2) only GPS data were processed in the kinematic mode, simulating real field conditions with a sampling rate of 1 s and elevation cutoff of 10°. Within this mode, the position parameters and receiver clock error are estimated at every epoch by the least-squares adjustment, while the phase ambiguities are estimated iteratively (Marques et al. 2016). Typically, this procedure leads to centimeter-level accuracy within 20 minutes, due to the convergence period of the phase ambiguity parameters (Gao and Shen 2002). In the presence of scintillation, PPP may experience higher-order errors mainly associated with cycle slips and range degradations in the observables. Using the RT-PPP software, if a cycle slip is detected through the algorithm designed by Blewitt (1990), its corresponding ambiguity parameter is re-initialized. Consequently, a new convergence period is required for such parameter and the accuracy of the positioning may deteriorate in the meanwhile. Another source of deterioration in positioning accuracy is the sudden change in geometry caused by losses of lock during scintillation, as highlighted by Zhang et al. (2014). The detection, identification and adaption (DIA) method (Teunissen 1998) is applied for outlier detection and quality control adjustment.

Typical examples of the influence of the alignment under discussion on the PPP performance is presented in Figures 8 and 9, based on data recorded between 19:00 LT and 21:00 LT during the night of 17 November 2014. Figure 8 shows the skyplot of the time variation of the IPPs of all available GPS satellite links to the São José dos Campos monitor, in combination with the corresponding S_4 values. The satellite signals transmitted by PRN18 (G18 in the plot) are associated with ray paths aligned with magnetic-field elongated EPBs between

20:06 LT and 21:00 LT, being persistently and severely affected by the strongest scintillation. However, the alignment condition actually started earlier at 19:35 LT, with little noticeable effects.

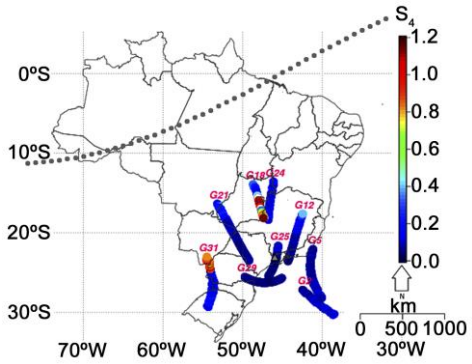

Fig. 8 Skyplot of the time variation of the IPPs of all available GPS satellite links to the São José dos Campos monitor in combination with the corresponding S_4 values for 17 November 2014 between 19:00 LT and 21:00 LT.

The upper three panels of Figure 9 present the total number of satellites used in the PPP solution, S_4 values for all satellites, and the noticeable cases of bit error probability $P_e > 10^{-6}$ (T_s < 20000 s). The bit error probability for the alignment condition, which only affected PRN18, started at approximately 20:06 LT and lasted until 21:00 LT, being indicated by red dots. However, the alignment precondition actually started at 19:35 LT, with lower P_e values. The bottom panel of Figure 9 displays the time series of the North, East and Up PPP error components. Analyzing the S_4 plot in Figures 9, it is observed that scintillation with $S_4 > 0.7$ started at 19:40 LT, so remaining until 21:00 LT, while the PPP solution experienced higher-order errors, reaching (and sometimes exceeding) meter-level accuracy between 20:35 LT and 20:47 LT. These events occurred simultaneously with the period of EPB alignment with the PRN18 propagation path, when noticeable values of P_e also occurred. This is an evidence that P_e is a realistic parameter to diagnose difficulties in the PPP processing approach, not only under alignment, where it is more perceptible, but also for $P_e > 10^{-6}$. What is quite relevant in the top

panel of Figure 9 is the fact that the transmissions by two satellites experienced simultaneous losses of lock during short intermittent intervals. These events are also identified by high P_e values, beginning at approximately 20:35 LT, according to corresponding panel of Figure 9. In the absence of adequate time for the PPP procedure to recover from losses of lock and converge again, its solution yields large errors.

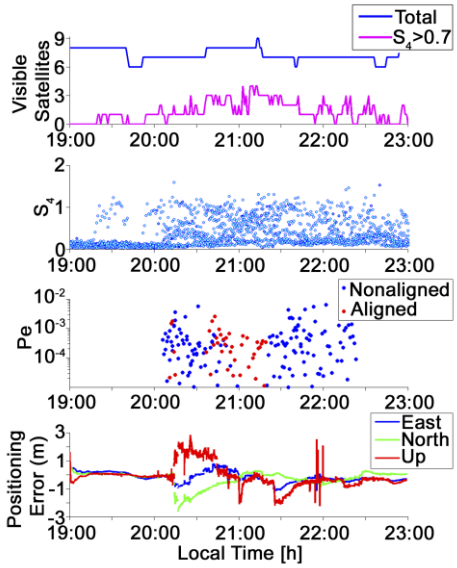

Figure 9 – Example from 17 November 2014. From top to bottom: total number of visible satellites used by the PPP processing approach; all S_4 values estimated between 19:00 LT and 23:00 LT; noticeable cases of bit error probability $P_e > 10^{-6}$ for aligned (red dots) and nonaligned cases (blue dots); and North (N), East (E) and Up (U) components of the positioning error calculated by the PPP processing approach.

Table 2 presents detailed results from the highlighted night of 17 November 2014 (DOY 321). It also presents observations for the period between 18 and 30 November, 2014. All alignment cases occurred for PRN18. The three-dimensional rms and average positioning error, calculated by the PPP processing approach, as well as its maximum value (all in m) are listed in

the last columns of Table 2, showing large PPP errors due to alignment. Such a result may be considered for mitigation of this type error in the future.

Table 2 PPP results under alignment conditions for 15-30 November 2014.

DOY	Cases $S_4 > 0.7$	Max(S_4)	Max(P_e)	RMS(3dσ)	Max(3dσ)	E(3dσ)
321	30	1.28	0.0027	0.3623	2.0304	0.3770
322	26	1.19	0.0047	0.4130	1.9380	0.5791
323	48	1.37	0.0025	0.3241	2.5973	0.4232
324	0	0.45	0.0000	0.1077	0.8250	0.3982
325	51	1.60	0.0036	0.9226	2.8496	0.9686
326	34	1.25	0.0030	0.3528	2.5637	0.6211
327	43	1.22	0.0031	0.1888	1.2140	0.3040
328	63	1.21	0.0035	0.1100	0.6216	0.3685
329	52	1.41	0.0030	0.1020	0.6263	0.2716
330	31	1.31	0.0012	0.1573	1.5378	0.5249
331	46	1.33	0.0049	0.1996	1.2328	0.8322
332	12	1.00	0.0014	0.2643	1.2503	0.7543
333	8	1.06	0.0054	0.3266	2.3209	0.7251
334	20	1.27	0.0013	0.4386	2.4038	1.2289

Conclusion

DasGupta et al. (2004) and Ray et al. (2014) previously demonstrated that GPS signals are more severely affected by scintillation when their propagation paths are aligned with EPBs. The former reference based their arguments on azimuth-elevation plots of the scintillation index

estimated from measurements performed by a GPS monitor located at Calcutta (22.58ºN, 88.38ºE geographic; 32.19ºN magnetic dip, 17.35ºN dip latitude), as well as on corresponding positioning errors, which reached 11 m in latitude and 8 m in longitude. The latter reference displayed S_4 values along GPS satellite tracks observed from Bhopal (23.28ºN, 77.34ºE geographic; 34.90ºN magnetic dip, 19.20ºN dip latitude) in combination with a map of the angle between the ray path and the geomagnetic field directions, in terms of the subionospheric latitude and longitude. Noting that the example also represented observations from several other stations in the Indian sector, the authors also arrived at the above conclusion. Here, experimental data obtained during 32 days at a station located under the Southern crest of the EIA in Brazil have been analyzed. The results have confirmed that, in the Brazilian sector, scintillation intensity is also enhanced when signal propagation path segments tend to align themselves with EPB structures, which are known to be elongated along magnetic flux tubes. Such scintillation enhancements occurred predominantly at azimuth angles around 345º, nearly aligned with the magnetic meridian over this region, which has a large westward declination (21.4º W). Moreover, that loss of phase lock is more likely to occur in the presence of this geometry. The present scenario favors the assessment of such effects. To extend the previous results, statistical analyses of the present experimental data have been performed. Next, the α-μ model has been used to estimate the mean time between cycle slips T_s through its approximate relationship with the bit error rate P_e of binary DPSK signals. Thus, it has been quantitatively shown that the above alignment, which resulted in more severe scintillation cases with high values of S_4, is also responsible for small values of T_s, likely causing losses of phase lock. The Precise Point Positioning analysis has shown that the large observed errors are related with that condition. The results has shown that PPP also experienced significant errors for high values of P_e, even in the absence of the alignment condition. In one particular example, these errors increased in response to transmissions by two satellites experiencing simultaneous losses of lock during short intermittent intervals. These events strongly impacted GPS availability and positioning performance. However, it has been shown that such performance metrics have been specially degraded under the alignment condition.

Acknowledgements: This work is supported by Conselho Nacional de Desenvolvimento Científico e Tecnológico (CNPq) under award number (INCT) 465648/2014-2. B. C. Vani thanks Federal Institute of Education, Science and Technology of Sao Paulo (IFSP) for supporting his PhD research and Coordenação de Aperfeiçoamento de Pessoal de Nível Superior (CAPES) for grant (CAPES/PDSE no. 19-2016/Process n. 88881.134266/2016-01). M. A. Abdu acknowledges the CAPES support for a senior visiting professorship at ITA/DCTA. E. Costa is supported by CNPq award number (PQ) 309013/2016-0. E. R. de Paula is supported by CNPq award number (PQ) 310802/2015-6. The monitoring stations were deployed in the context of Projects CIGALA/CALIBRA, funded by the European Commission (EC) in the framework of FP7-GALILEO-2009-GSA and FP7–GALILEO–2011–GSA–1a, respectively, and FAPESP Project Number 06/04008-2. The authors thank the reviewers for the insightful and constructive comments, which helped them in the development of a better paper.

References

Abdu, M. A.; Bittencourt, J. A. Batista, I. S. (1981). Magnetic declination control of the equatorial F region dynamo electric field development and spread F. J. Geophys. Res., 86(13), pp.11443–11446, doi:10.1029/JA086iA13p11443.

Abdu, M. A.; Kherani, E. A.; Batista, I. S.; de Paula, E. R.; Fritts, D. C. Sobral, J. H. A. (2009). Gravity wave initiation of equatorial spread F/plasma bubble irregularities based on observational data from the SpreadFEx campaign. Annales Geophysicae, 27, pp. 2607-2622, doi: 10.5194/angeo-27-2607-2009.

Abdu, M. A., Brum, C. G. M., Batista, P. P., Gururbaran. S., Pancheva, D., Bageston, J. V., Batista, I. S., Takahashi, H. (2015). Fast and ultrafast Kelvin wave modulations of the equatorial evening F region vertical drift and spread F development. Earth, Planets and Space, 67, pp. 1-15, doi: 10.1186/s40623-014-0143-5.

..Basu, S. and S. Basu (1981). Equatorial scintillations - a review, Journal of Atmospheric and Terrestrial Physics, 43 (5-6), pp. 473-489, doi:10.1016/0021-9169(81)90110-0.

Formatted: Portuguese (Brazil)

Formatted: Portuguese (Brazil)

Formatted: English (United States)

Blewitt, G. (1990). An automatic editing algorithm for GPS data. Geophysical Research Letters, 17(3), pp. 199-202, doi:10.1029/GL017i003p00199.

DasGupta, A., S. Ray, A. Paul, P. Banerjee, Bose, A. (2004), Errors in position-fixing by GPS in an environment of strong equatorial scintillations in the Indian zone, Radio Sci., 39, RS1S30, doi:10.1029/2002RS002822.

de Paula E. R., Jonah O. F., Moraes A. O., Kherani E. A., Fejer B.G., Abdu M. A., Muella M. T. A. H., Batista I. S., Dutra S.L. G., Paes R. R. (2015) Low-latitude scintillation weakening during sudden stratospheric warming events. J. Geophys. Res., 120, pp. 2212-2221, doi: 10.1002/2014JA020731.

Doherty, P. H., Delay, S. H., Valladares, C. E., Klobuchar, J. A. (2004). Ionospheric Scintillation Effects on GPS in the Equatorial and Auroral Regions. J. Inst. of Navig., *50*(4), pp. 235-246, doi: 10.1002/j.2161-4296.2003.tb00332.x.

El Ayadi, M. M. H. and Ismail, M. H. (2014). Novel Closed-Form Exact Expressions and Asymptotic Analysis for the Symbol Error Rate of Single- and Multiple-Branch MRC and EGC Receivers Over α-μ Fading. IEEE Trans. Veh. Technol., 63 (9), pp. 4277-4291, doi: 10.1109/TVT.2014.2316418.

Gao, Y. and X. Shen (2002). A New Method for Carrier-Phase-Based Precise Point Positioning. J. Inst. of Navig., 49 (2), pp. 109-116, doi: 10.1002/j.2161-4296.2002.tb00260.x.

Humphreys, T. E., Psiaki, M. L., Hinks, J. C., O'Hanlon B., Kintner, P. M. (2009). Simulating Ionosphere-Induced Scintillation for Testing GPS Receiver Phase Tracking Loops. IEEE J Sel Top Signal Process, 3 (4), pp. 707-715, doi: 10.1109/JSTSP.2009.2024130.

Humphreys, T. E., Psiaki, M. L., Ledvina, B. M., Cerruti, A. P., Kintner, P. M. (2010a). Data-Driven Testbed for Evaluating GPS Carrier Tracking Loops in Ionospheric Scintillation. IEEE Trans Aerosp Electron Syst, 46 (4), pp. 1609-1623, doi: 10.1109/TAES.2010.5595582.

Humphreys, T. E.; Psiaki, M. L. and P. M. Kintner, Jr. (2010b). Modeling the Effects of Ionospheric Scintillation on GPS Carrier Phase Tracking. IEEE Trans. Aerosp. Electron. Syst., 46 (4), pp. 1624-1637, doi: 10.1109/TAES.2010.5595583.

Kintner, P. M., Kil, H., Beach, T. L., de Paula, E. R. (2001), Fading timescales associated with GPS signals and potential consequences, Radio Sci., 36(4), 731–743, doi:10.1029/1999RS002310.

Kintner, P. M., Ledvina, B. M., de Paula, E. R. (2007). GPS and ionospheric scintillations. Space Weather, *5* (S09003), pp. 1-23, doi:10.1029/2006SW000260.

Marques, H. A., Monico, J. F. G., Shimabukuro, M. H., Oyama, R. T., Wentz, J. P. (2014). Real Time PPP: Fundamentals, Computational Implementation and Results Analysis for Static and Kinematic Mode. Brazilian Cartography Magazine (Revista Brasileira de Cartografia), 6 (66), pp. 1331-1345, ISSN: 1808-0936.

Marques, H. A. S., Monico, J. F. G., Marques, H. A. (2016). Performance of the L2C civil GPS signal under various ionospheric scintillation effects. GPS Solut., 20 (2), pp. 139-149, doi:10.1007/s10291-015-0472-2.

Moraes, A. O., de Paula, E. R., Perrella, W. J. Rodrigues, F. S. (2012). On the distribution of GPS signal amplitudes during the low-latitude ionospheric scintillation. GPS Solut., 17 (4), pp. 499-510, doi:10.1007/s10291-012-0295-3.

Moraes, A. O., de Paula, E. R., Muella, M. T. A. H., Perrella, W. J. *(*2014a*).* On the second order statistics for GPS ionospheric scintillation modeling. Radio Sci., 49 (2), *pp.* 94-105, *doi:*10.1002/2013RS005270.

Moraes, A. O., Costa, E., de Paula, E. R., Perrella, W. J., Monico, J. F. G. (2014), Extended ionospheric amplitude scintillation model for GPS receivers, Radio Sci., 49, 315–333, doi:10.1002/2013RS005307.

Moraes, A. O., Costa, E., Abdu, M. A., Rodrigues, F. S., de Paula, E. R., Oliveira, K., Perrella, W. J. (2017), The variability of low-latitude ionospheric amplitude and phase scintillation detected by a triple-frequency GPS receiver, Radio Sci., 52, 439–460, doi:10.1002/2016RS006165.

Moreno, B., Radicella, S., De Lacy, M. C., Herraiz, M. Rodriguez-Caderot, G. (2011). On the effects of the ionospheric disturbances on precise point positioning at equatorial latitudes. GPS Solut., 15(4), pp. 381-390, doi:10.1007/s10291-010-0197-1.

Magableh, A. M. Matalgah, M. M. (2009). Moment generating function of the generalized α - μ distribution with applications. IEEE Comm. Let., 13 (6), pp. 411-413, doi: 10.1109/LCOMM.2009.090339.

Sobral, J. H. A., Abdu, M. A., Takahashi, H., Taylor, M. J, de Paula, E. R., Zamlutti, C. J., Aquino, M. G., Borba, G. (2002). Ionospheric plasma bubble climatology over Brazil based on 22 years (1977-1998) of 630 nm airglow observations. J. Atmos. Sol. Terr. Phys., 64 (12-14), pp. 1517-1524, doi: 10.1016/S1364-6826(02)00089-5.

Ray, S., Bhowmik, U., and Das, A. (2014), Scintillation effects related to propagation geometry as applicable to Indian SBAS, Proceedings of the XXXI URSI General Assembly and Scientific Symposium, paper 1463, Beijing, China.

Teunissen, P. J. G. (1998). Quality control and GPS. In: Teunissen, P. J. G., Kleusberg, A. (eds.), GPS for geodesy, 2nd ed. Springer, Berlin, pp 271–318.

Formatted: English (United States)

Tsunoda, R. T. (1985). Control of the seasonal and longitudinal occurrence of equatorial scintillations by the longitudinal gradient in integrated E region Pederson conductivity. J Geophys Res., 90 (A1), pp. 447-456, doi: 10.1029/JA090iA01p00447.

Thébault, E.; et al. (2015). International Geomagnetic Reference Field: the 12th generation. Earth, Planets and Space, 67:79, pp. 1-19, doi: 10.1186/s40623-015-0228-9.

Vani, B. C., Shimabukuro, M. H. Monico, J. F. G. (2016). Visual exploration and analysis of ionospheric scintillation monitoring data: The ISMR query tool. Comp. & Geosc., 104, pp.125-134, doi: 10.1016/j.cageo.2016.08.022.

Xu, R., Liu, Z., Li, M., Morton, Y., Chen, W. (2012). An analysis of low-latitude ionospheric scintillation and its effects on precise point positioning. Journal of Global Positioning Systems, 11(1). Pp. 22-32, doi: 10.5081/jgps.11.1.22.

Yacoub, M. D. (2007). The α-μ distribution: A physical fading model for the Stacy distribution. IEEE Trans Veh Technol, 56 (1), pp. 27-34, doi:10.1109/ TVT.2006.883753.

Yeh, K. C. and Liu, C. H. (1982). Radio wave scintillations in the ionosphere, Proceedings of the IEEE, 70 (4), pp. 324-360, doi:10.1109/PROC.1982.12313.

Zhang, X., Guo, F., Zhou, P. (2014). Improved precise point positioning in the presence of ionospheric scintillation. GPS Solut, 18 (1), pp. 51-60, doi:10.1007/s10291-012-0309-1.

Zumberge, J. F., Heflin, M. B., Jefferson, D. C., Watkins, M. M., Webb, F. H. (1997). Precise point positioning for the efficient and robust analysis of GPS data from large networks. J Geophys Res., 102 (B3), pp. 5005-5017, doi: 10.1029/96JB03860.

Author Biographies

Alison Moraes received the B.S. in telecommunications engineering from Universidade de Taubaté, UNITAU, Brazil in 2003, and Dr. Sc degree in the school of Electronic and Computer Engineering at

Formatted: Portuguese (Brazil)

Formatted: English (United States)

Instituto Tecnológico de Aeronáutica, ITA, Brazil in 2013. Engineer at the Instituto de Aeronáutica e Espaço IAE since 2004, and graduate professor at ITA since 2015.

Bruno Vani: Received the B.S. in Computer Science (2011) and M. Sc. (2014) in Cartographic Sciences from Univ. Estadual Paulista (UNESP). Currently he is a PhD candidate at UNESP. Since 2014, he is a lecturer at the Instituto Federal de São Paulo (IFSP/SP), Presidente Epitácio, Brazil.

Emanoel Costa: received the BS and MS degrees in electrical engineering from Instituto Militar de Engenharia, Brazil in 1972 and 1974, and the Ph. D. degree from Cornell University, USA, in 1978. He has been with CETUC/PUC-Rio, Brazil, since 1978, with research interests in the areas of tropospheric and ionospheric effects on radio wave propagation.

Mangalathayil Abdu: Received Ph.D. degree, in 1967, from Gujarat University India. He has been postdoctoral research fellow at the University of Western Ontario (1968- 71), professor at CRAAM Mackenzie University, Sao Paulo (1971-73), research scientist since 1973 at the National Institute for Space Research (INPE), and presently a visiting professor at ITA. His research interests are in space weather and Ionospheric physics..

Eurico de Paula: attended the M. Sc. degree at Telecommunications at ITA, and Dr. Sc. in Geophysics at INPE, where he has been working as a Researcher for 40 years. He attended pos-doc programs at USU, Utah State University, Logan, USA for 5 years. His main area of interest is ionospheric physics with focus on ionospheric scintillations detected by radars and GPS receivers.

Jonas Sousasantos: Graduated in Mathematics at the Universidade de Taubaté, UNITAU, Brazil in 2010. Dr. Sc. (2017) and M. Sc. (2013) degrees obtained at the National Institute for Space Research. He is currentely a Postdoctoral Associate at Instituto Tecnológico de Aeronáutica, ITA. His main area of interest is mathematical modeling and forecasting of ionospheric irregularities and atmospheric-ionospheric vertical coupling.

Galera Monico: Graduated in Cartographic Eng. from UNESP (1982), master in Geodetic Science from UFPR (1988) and Ph.d. on Space Geodesy from Nottinhgam Univeristy (1995). Has experience in Geosciences, focusing on the following subjects: GNSS for Geodesy and Atmosphere, Quality Control on Geodesy. Dr. Galera Monico was indicated as one of the 50 GNSS Leaders to Watch by the GPS World magazine.

Biagio Forte: Dr graduated in Physics at the University of Trieste (Italy) and went on to complete a PhD in Geo-Physics at the Karl-Franzens University of Graz (Austria). Biagio joined the Department of Electronic and Electrical Engineering in 2012 as a Prize Fellow in Space Weather.

Patricia Negreti: Graduated in Physics from Universidade Estadual Paulista Júlio de Mesquita Filho (2003), where he received 4 awards/honors. Masters in Medical Physics by the Institute of Energy and Nuclear Research (2006) and PhD in Space Geophysics by the National Institute of Space Research (2012).

Milton Shimabukuro: Assistant Professor at UNESP, Presidente Prudente, São Paulo, Brazil, since 2006. He received B.S. degree in Computer Science and doctorate in Computer Science and Computational Mathematics, both from Institute of Mathematics and Computer Sciences, University of São Paulo, Brazil. His research interests are visual analytics, organization and visualization of spatial and temporal data.